Combustion and Flame 260 (2024) 113267

Contents lists available at ScienceDirect

Combustion and Flame

journal homepage: www.sciencedirect.com/journal/combustion-and-flame

Enhanced C2-CN sub-mechanism: Impact on NO/N_2O and soot precursor yields during C_2H_2/HCN oxidation

Yu Yang [a], Shu Zheng [a,*], Huanhuan Wang [b], Bin Hu [a], Hao Liu [a], Ran Sui [b], Qiang Lu [a,*]

[a] National Engineering Research Center of New Energy Power Generation, North China Electric Power University, Beijing 102206, PR China
[b] Center for Combustion Energy, Department of Energy and Power Engineering, Tsinghua University, Beijing 100084, PR China

ARTICLE INFO

Keywords:
C2-CN sub-mechanism
hydrocarbon-ammonia fuels
polycyclic aromatic hydrocarbon (PAHs)
NO emission
barrierless reaction

ABSTRACT

The combustion of hydrocarbon-ammonia fuels poses challenges related to the formation of soot and nitrogen oxides (NOx) emissions. Various kinetic mechanisms have been developed to describe the pathways of soot and NOx formation, but limited attention has been paid to the role of the C2-CN species, such as HC_3N and CH_2CHCN, in influencing the yields of soot and NOx. To address this gap, we present a detailed C2-CN sub-mechanism integrated into a NOx and polycyclic aromatic hydrocarbons (PAHs) kinetic model. The rate constants of the barrierless association reactions of C_2H+CN, C_2H_3+CN, C_2H_5+CN, and CH_3+CH_2CN were updated using the variable reaction coordinate transition state theory (VRC-TST). We numerically investigated the oxidation of C_2H_2 and HCN at equivalence ratios of 2.0 and 3.0, which are major precursors for NOx and PAHs, in a perfectly stirred reactor (PSR) employing two kinetic models (with/without the developed C2-CN sub-mechanism). By comparing the rates of production (ROPs) obtained via both models, we analyzed the formation pathways of NO/N_2O and Benzo(ghi)fluoranthene (BGHIF). Our findings reveal temperature-dependent trends in the calculated rate constants of C_2H_5+CN and CH_3+CH_2CN associations (positive dependence) as well as C_2H+CN and C_2H_3+CN associations (negative dependence). The peak mole fractions of BGHIF at equivalence ratio (φ) of 2.0 and 3.0 predicted by the updated mechanism were 18.4 % and 13.6 % lower than the base mechanism. This reduction can be attributed to an additional consumption channel of C_2H_2 (C_2H_2+CN=HC_3N+H) predicted by the C2-CN sub-mechanism. Furthermore, the C2-CN sub-mechanism exhibited a stronger suppression effect on N_2O formation compared with NO formation at φ=2.0 and 3.0. This limitation can be explained by an additional consumption channel of CN via CN+C_2H_2=HC_3N+H, resulting in decreased NO/N_2O through the reaction sequence CN→NO→N_2O and CN→NCO→HNCO→NH_2→HNO→NO→N_2O.

Novelty and Significant

Using variable reaction coordinate transition state theory, this work developed a new sub-mechanism for C2-CN species, which are key intermediates for soot and NOx formation in hydrocarbon/NH_3 combustion. The formation pathways of C2-CN species in C_2H_2/HCN oxidation were revealed for the first time, and their effects on the formation pathways of soot and NOx precursors were elucidated. Including the C2-CN sub-mechanism in the chemical kinetic mechanisms resulting in significant decrease of mole fractions of five-ring polycyclic aromatic hydrocarbons (PAHs) and N_2O. The most important reactions in the C2-CN sub-mechanism that reduced the mole fractions of five-ring PAHs and N_2O were identified through the analysis of rate of production (ROP).

1. Introduction

The combustion of hydrocarbon fuels contributes significantly to the greenhouse effect and global warming through carbon dioxide emissions. To mitigate global warming, it is crucial to explore alternative fuels such as hydrogen (H_2). However, the storage and transportation of H_2 at a low cost pose challenges due to its extremely low boiling point. As a carbon-free fuel, ammonia (NH_3) only produces nitrogen and water during complete combustion. Furthermore, NH_3 can be liquified at 1.0 MPa under atmospheric temperature [1], which makes it an economically viable energy storage medium. Therefore, NH_3 is emerging as an attractive alternative fuel to hydrocarbon fuels.

One effective approach to enhance the low burning velocity of NH_3 is to blend it with hydrocarbon fuels [2], but soot formation remains a

* Corresponding authors.
E-mail addresses: andy123zhengshu@sina.com (S. Zheng), qianglu@mail.ustc.edu.cn (Q. Lu).

https://doi.org/10.1016/j.combustflame.2023.113267
Received 30 July 2023; Received in revised form 16 December 2023; Accepted 17 December 2023
Available online 21 December 2023

challenge. Additionally, the emission of fuel-NOx during NH_3 combustion is another drawback [3]. Understanding the detailed mechanisms of soot and NOx formation provides a theoretical foundation for developing strategies to cut soot and NOx emissions in NH_3/hydrocarbon fuel combustion.

Numerous studies conducted over the past two decades have aimed to elucidate the mechanism of soot formation. The consensus derived from these studies is that soot formation primarily involves the generation of benzene (A1) and polycyclic aromatic hydrocarbons (PAHs), soot inception, soot condensation, and H-abstraction and C_2H_2-addition (HACA) surface growth. The generation of A1 is considered the initial step in the formation of PAHs, described by reactions between C_2H_2 and C_4H_x species [4] or the combination of two C_3H_3 [5]. Soot inception can be modeled by the collision of two pyrenes (A4s) or five-ring PAHs (A5s), which have been successfully applied in C_2H_4 [6,7] and CH_4 [8] co-flow flames. Soot condensation, a significant process contributing to increased soot loadings, is assumed to occur through the collision of soot and PAHs [9]. The HACA surface growth mechanism, updated by APPEL and BOCKHORN [10], is widely employed to predict soot volume fractions (SVF) in various laminar C_2 hydrocarbon-fuel flames [11,12].

Previous studies have also investigated NH_3 oxidation chemistry. Miller and Bowman [13] systematically developed a mechanism for the conversion of NH_3 to NO. They determined that the primary consumption of NH_3 occurred through the H-abstraction by the OH radical ($NH_3+OH=NH_2+H_2O$). Klippenstein et al. [14] incorporated the NNH mechanism into the NH_3 oxidation mechanism using *ab initio* methods. Their findings revealed that $NNH+O=NH+NO$ played a significant role in enhancing the accuracy of NO concentration predictions. In line with the Klippenstein mechanism, Song et al. [15] adopted *ab initio* methods to calculate the reaction rate of H_2NO+O_2, aiming to better match the experimental NO concentration during NH_3 oxidation under high pressures.

Besides the aforementioned studies, it has been indicated by Refs. [11,16] that the formation pathways of soot and NOx are influenced by the interaction between nitrogen and hydrocarbons, which should be identified and considered. Konnov et al. [17] developed a detailed C/H/N/O reaction mechanism incorporating C—N chemistry to predict NOx formation in CH_4/NH_3 flames. The NOx modeling exhibited good agreement with experimental results in lean flames (at equivalence ratio of 0.7–0.9), but significant discrepancies were observed in rich flames (at equivalence ratio of 1.1–1.3). Mendiara and Glarborg [18] updated a detailed chemical mechanism for CH_4/NH_3 flames, incorporating CH_xNH_y and CH_xCN_y reactions. This mechanism successfully captured the trends of NO concentrations in both lean and rich flames. Glarborg et al. [19] synthesized nitrogen chemistry, including the oxidation of CN-compounds like HCN and HNCO, and validated it in the jet-stirred reactors and laminar premixed flames.

Despite the satisfactory performance of the C—N mechanism in predicting NOx in NH_3/hydrocarbon flames, Montgomery et al. [20] discovered that this mechanism was unable to fully capture the trends of SVF in NH_3/CH_4 flames. The deficiency primarily stemmed from the absence of reactions between C3-hydrocarbons and NH_3, as well as their decomposition products. Bennett et al. [11] reached a similar conclusion in C_2H_4/NH_3 flames, detecting the presence of C2-CN compounds such as H_3C_3N. However, due to the unclear formation pathways of these C2-CN compounds, it remains challenging to elucidate the suppressive effect of NH_3 on soot formation.

Several studies have attempted to establish the C2-CN mechanism. Herbert et al. [21] conducted experimental investigations to determine the rate constants of the associations of CN with C_2H_2, C_2H_4, and C_2H_6 at 295~700 K. Albernaz et al. [22] extended the $CN+C_2H_2$ reaction rates to 200–3000 K using *ab initio* calculations with the CCSD (T)/aug-cc-pCVTZ method. Pelucchi et al. [23] presented an extension of the combustion kinetics of pyrrole (C_4H_5N) that included reactions involving C2-CN compounds. Their results demonstrated good agreement between the mole fraction of CH_2CHCN and experimental values. Wu et al. [24] utilized the C2-CN mechanism developed by Mackie et al. [25] to explain the formation pathway of CH_2CHCN observed during the experimental oxidation of pyridine (C_5H_5N). However, very few studies have specifically investigated the effect of the C2-CN mechanism on the soot/NOx formation in NH_3/hydrocarbon flames. Additionally, the reaction rates of certain radical-radical association reactions, such as $C_2H_3+CN=CH_2CHCN$ and $C_2H_5+CN=C_2H_5CN$ [26], were estimated in Ref. [24]. These reactions pose challenges to calculation based on classical transition state theory (CTST) due to their barrierless nature [27]. Barrierless association reactions play a significant role in combustion chemistry [28], and accurately estimating their temperature-dependent rate constants is the foundation for investigating combustion characteristics. The variable reaction coordinate transition state theory (VRC-TST), developed specifically for calculating rate constants of barrierless reactions, has shown good performance in predicting rate constants for the barrierless association of two CF_2 [28] and the association of Cl with C_2H_2 [29].

This study aims to quantitatively evaluate the impact of the C2-CN sub-mechanism on soot and NO/N_2O formation during the oxidation of C_2H_2/HCN. First, the reaction rates of certain barrierless reactions were updated using VRC-TST with the potential surface calculated by direct dynamics using M06–2X/def2-TZVP. Second, a new kinetic model that combines the updated C2-CN sub-mechanism with the mechanisms of soot/NOx formation was developed. The oxidation of C_2H_2/HCN in a perfectly stirred reactor (PSR) at different equivalence ratios was simulated using the mechanism with and without the C2-CN sub-mechanism to investigate its effect on the soot/NOx formation. C_2H_2 was chosen to represent C-compounds since it dominates the formation of benzene and the HACA mechanism. HCN was selected as the representative N-compound due to its significant role in the formation of NO/N_2O [30] and C2-CN compounds [31,32].

2. Computational details

Two new kinetic models were established for the oxidation of NH_3/hydrocarbon fuels. One was referred to as the updated mechanism, incorporated the C2-CN sub-mechanism, while the other model, referred to as the base mechanism, did not include the C2-CN sub-mechanism. The base mechanism was developed from Pelucchi et al. [23] (C0-C2 species sub-mechanism, N-containing species sub-mechanism, and C1/C2-N species sub-mechanism) and Slavinskaya et al. [33] (C3-C5 species and aromatics sub-mechanism). Additionally, reactions involving HCN from the Pelucchi mechanism [23] were replaced with those developed by Capriolo et al. [34].

The updated mechanism resulted from merging the base mechanism with the C2-CN sub-mechanism, primarily derived from Pelucchi et al. [23], Wu et al. [24], and Lifshitz and Tamburu [35], as detailed in Table 1.

The rate constants of four barrierless reactions, i.e., $C_2H+CN=HC_3N$, $C_2H_3+CN=CH_2CHCN$, $C_2H_5+CN=C_2H_5CN$, and $CH_3+CH_2CN=C_2H_5CN$, were recalculated in this study using the VRC-TST. The VRC-TST calculations were conducted using the POLYRATE program [36] with the GAUSSRATE interface to Gaussian 16 [37], using M06–2X/def2-TZVP [38,39]. For each reaction, the pivot points were positioned at 0.1 Å from the center of bonding atoms. The minimum *E, J* resolved rate constants at a sequence of reaction coordinate values *s* from 1.4 to 4.4 Å (with a step size of 0.2 Å) were calculated. For each value of *s*, the vibrational-rotational accessible states were evaluated by Monte Carlo integration with 640 geometric configurations.

Once the rate constants at different temperatures were obtained, the modified Arrhenius equation was adopted [40]:

$$k(T) = AT^n \exp(-E/RT)$$

The oxidation of C_2H_2/HCN was simulated in a PSR at 700~1500 K and 1 atm using the OpenSMOKE++ software [41]. The reactor had a diameter of 5.0 cm. The initial mole fractions of the gas mixture

Table 1
The C2-CN sub-mechanism, rate constants were given as $k = AT^n\exp(-E/RT)$ (Units are cal, mol, K, cm, and s.).

Reaction	A	n	E	Source
R1: CHCHCN+CN = HC_3N+HCN	1.0E14			[24]
R2: CHCHCN+H = HC_3N+H_2	4.0E13			[24]
R3: H+CHCHCN=CH_2CHCN	4.0E13			[23]
R4: 2CHCHCN=CH_2CHCN+HC_3N	1.0E50	−10.50	67,965	[23]
R5: CHCHCN=H+HC_3N	1.0E12		47,970	[23]
R6: H+HC_3N=C_2H_2+CN	1.0E14		2000	[23]
R7: C_2H+CN=HC_3N	1.9E13	0.33	−368	pw.
R8: O+HC_3N=HCCO+CN	3.0E09	1.28	2472	[23]
R9: O+HC_3N=CO+HCCN	7.4E08	1.28	2472	[23]
R10: OH+HC_3N=CH_2CO+CN	7.5E06	1.55	2106	[23]
R11: H+CH_2CHCN=H_2+CHCHCN	1.1E07	1.93	12,950	[23]
R12: OH+CH_2CHCN=H_2O+CHCHCN	5.5E03	2.75	2216	[23]
R13: O+CH_2CHCN=OH+CHCHCN	4.7E06	2.00	8058	[23]
R14: O_2+CH_2CHCN=HO_2+CHCHCN	2.1E13		57,623	[23]
R15: HO_2+CH_2CHCN=H_2O_2+CHCHCN	3.2E06	2.00	24,888	[23]
R16: CH_3+CH_2CHCN=CH_4+CHCHCN	1.2E05	2.00	10,078	[23]
R17: CH_2CHCN=HC_3N+H_2	1.3E13		77,000	[24]
R18: OH+CHCHCN=C_2H_2+HNCO	1.0E12		5000	[23]
R19: O+CHCHCN=C_2H_2+NCO	1.0E12		5000	[23]
R20: CHCHCN=C_2H_2+CN	5.0E13		59,962	[23]
R21: C_2H_3+CH_2CHCN=C_2H_4+CHCHCN	1.5E13		10,003	[23]
R22: CHCHCN+H = HCN+C_2H_2	3.1E13			[24]
R23: CHCHCN+M=H+C_3HN+M	8.0E15		40,000	[23]
R24: CH_2CH_2CN=H+CH_2CHCN	3.1E13		36,574	[23]
R25: 2CH_2CN = CH_2CHCN+HCN	1.0E13		4000	[24]
R26: C_2H_5CN=H_2+C_2H_3CN	2.5E13		77,000	[35]
R27: C_2H_4CN+CH_3=CH_4+C_2H_3CN	2.5E11		9000	[35]
R28: H+CH_2CHCN=C_2H_3+HCN	5.0E12		8003	[23]
R29: OH+CH_2CHCN=>C_2H_3+HCNO	3.0E12		10,000	[23]
R30: CH_2CHCN=C_2H_2+HCN	2.6E12	0.10	75,968	[23]
R31: C_2H_3+CN=CH_2CHCN	9.1E13	0.14	−159	pw.
R32: H+CH_2CHCN=CH_3CHCN	5.0E12		4706	[23]
R33: O+CH_2CHCN=C_2H_2+HCNO	1.0E12		5000	[23]
R34: OH+CH_2CHCN=>CH_3CHO+CN	3.0E12		7000	[23]
R35: O+CH_2CHCN=C_2H_3+NCO	3.0E09	1.18	8130	[23]
R36: C_2H_5CN=H+CH_2CH_2CN	1.0E15		97,946	[23]
R37: H+C_2H_5CN=H_2+CH_2CH_2CN	6.3E13		7000	[23]
R38: CH_3+C_2H_5CN=CH_4+CH_2CH_2CN	1.0E12		8003	[23]
R39: CH_2CN+C_2H_5CN=CH_3CN+CH_2CH_2CN	5.0E12		22,981	[23]
R40: OH+C_2H_5CN=H_2O+CH_2CH_2CN	1.0E00	3.87	−100	[23]
R41: CH_2CH_2CN=C_2H_4+CN	1.8E15		59,962	[23]
R42: C_2H_5CN=═H+CH_3CHCN	1.5E15		91,949	[23]
R43: H + C_2H_5CN═H_2+CH_3CHCN	6.3E13		6593	[23]
R44: CH_3+C_2H_5CN═CH_4+CH_3CHCN	1.0E12		8003	[23]
R45: CH_2CN+C_2H_5CN═CH_3CN+CH_3CHCN	5.0E12		27,998	[23]
R46: CH_3CHCN═CH_3+HCCN	1.0E13		89,967	[23]
R47: C_2H_5CN=C_2H_4+HCN	6.0E12		72,000	[35]
R48: C_2H_5+CN═C_2H_5CN	1.3E13	0.40	−1700	pw.
R49: CH_3+CH_2CN═C_2H_5CN	3.4E10	0.06	−1700	pw.
R50: OH+C_2H_5CN=C_2H_5+HOCN	1.2E01	3.50	−621	[23]
R51: OH+C_2H_5CN=C_2H_5+HNCO	7.2E-17	10.05	318	[23]
DUPLICATE	2.7E15	0.78	17,857	
OH+C_2H_5CN=C_2H_5+HNCO				
DUPLICATE				

C_2H_2/HCN/O_2 were provided in Table 2. Argon (Ar) was used as the diluent gas.

3. Results and discussion

Fig. 1 illustrates the calculated rate constants for the associations of C_2H+CN, C_2H_3+CN, C_2H_5+CN, and CH_3+CH_2CN, along with the comparison to those estimated by Pelucchi et al. [23]. As depicted in Fig. 1, the calculated rate constants of C_2H_5+CN and CH_3+CH_2CN exhibited a positive dependence on temperature. The calculated rate constants for C_2H_5+CN were approximately one order of magnitude higher than those reported by Pelucchi et al. [23]. Conversely, the calculated rate constants for CH_3+CH_2CN were around two orders of magnitude lower than the predictions of Pelucchi et al. [23]. In contrast to the C_2H_5+CN and CH_3+CH_2CN, the calculated rate constants for C_2H+CN and C_2H_3+CN displayed a negative correlation with temperature, although the temperature dependence was much weaker. Furthermore, the calculated rate constants for C_2H+CN and C_2H_3+CN were approximately 3∼4 times higher than those by Pelucchi et al. [23].

Table 2
The inlet mole fractions of C_2H_2, HCN, and O_2.

Case	C_2H_2	HCN	O_2	Ar	Equivalence ratio (φ)
1	0.004	0.004	0.0085	0.9835	2.0
2	0.004	0.004	0.0057	0.9863	3.0

3.1. Validation of models

The oxidation of C_4H_5N in a JSR at the temperature range of 700–1200 K, as conducted by Pelucchi et al. [23] was modeled using both the base and updated mechanisms. Fig. 2 compares the mole

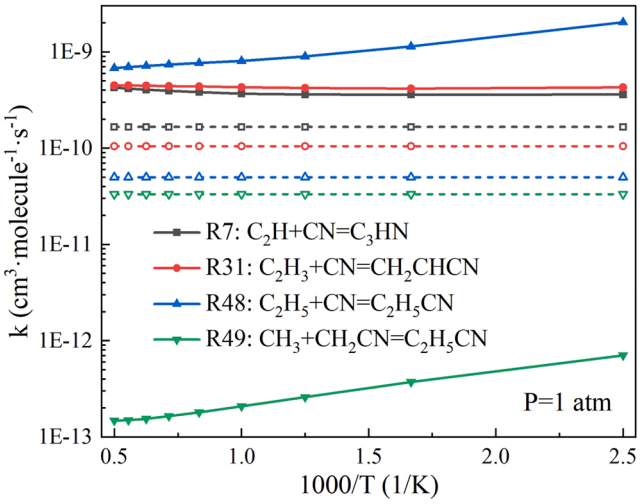

Fig. 1. Rate constants for C_2H+CN, C_2H_3+CN, C_2H_5+CN, and CH_3+CH_2CN associations, solid lines indicate rate constant calculated by the VRC-TST and dash lines represent rate constant from Pelucchi et al. [23].

fractions of C_4H_5N, O_2, C_2H_2, HCN, CH_3CN, and CH_2CHCN calculated with the two mechanisms. In Fig. 2(a), during the initial stage (700~750 K) of C_4H_5N oxidation, the mole fractions of C_4H_5N and O_2 calculated with base and updated mechanisms were almost the same. While in the fast pyrolysis stage (750~1000 K), the mole fractions of C_4H_5N and O_2 calculated with updated mechanism were higher, approaching the experimental results. In Fig. 2(b), compared to the experimental mole fraction of C_2H_2, the base mechanism significantly overpredicted the peak mole fraction by 1.36×10^{-4}, whereas the updated mechanism performed better, with a relative difference of 0.55×10^{-4}. The peak mole fraction of CH_3CN calculated with the updated mechanism was 5.55×10^{-5}, aligning more closely with the experimental results (5.68×10^{-5}) compared to the base mechanism (4.87×10^{-5}). The peak mole fraction of HCN calculated by the updated mechanism was approximately 64.5 % higher than that by the base mechanism, closer to the experimental peak mole fraction of HCN. In Fig. 2(c), at an equivalence ratio of 1.0, the base mechanism overpredicted the peak mole fraction of CH_2CHCN by 0.84×10^{-4}, while the updated mechanism underpredicted it by 2.1×10^{-4}. In the base mechanism, only the formation channel of CH_2CHCN was considered, resulting in an overestimation of the mole fraction of CH_2CHCN. While the absence of the consumption channel of CH_2CHCN in the base mechanism provides a better prediction of the peak mole fraction at an equivalence ratio of 1.0 compared to the updated mechanism, the predicted peak mole fraction of CH_2CHCN with base mechanism at the equivalence ratio of 2.0 was approximately 3 times higher than the experimental result. The calculated peak mole fraction of CH_2CHCN with updated mechanism at the equivalence ratio of 2.0 was 6.05×10^{-4}, in good agreement with the experimental result (6.58×10^{-4}). In summary, the updated mechanism demonstrated better performance in predicting C_4H_5N oxidation compared to the base mechanism.

To validate the rate constants of four barrierless reactions calculated with VRC-TST, the mole fractions of C_4H_5N, O_2, and CH_2CHCN in C_4H_5N oxidation at φ=1.0 were compared using the rate constants from both this study and those in [23] as shown in Fig. 3. In Fig. 3, at equivalence ratio of 1.0, the calculated mole fractions of C_4H_5N and O_2 using the rate constants obtained in this study closely matched those obtained in [23]. The peak mole fraction of CH_2CHCN calculated using the rate constants from [23] was 2.69×10^{-4}. When adopting the rate constants calculated in this study, the peak mole fraction of CH_2CHCN increased to 2.84×10^{-4}, approaching the measured result (4.94×10^{-4}).

Fig. 4 compares the experimental and modeling results for the oxidation of HCN in a plug flow reactor. Since HCN oxidation did not generate large amount of C2 species [42], the effect of C2-CN sub--mechanism on the predictions of products was limited. Hence, the

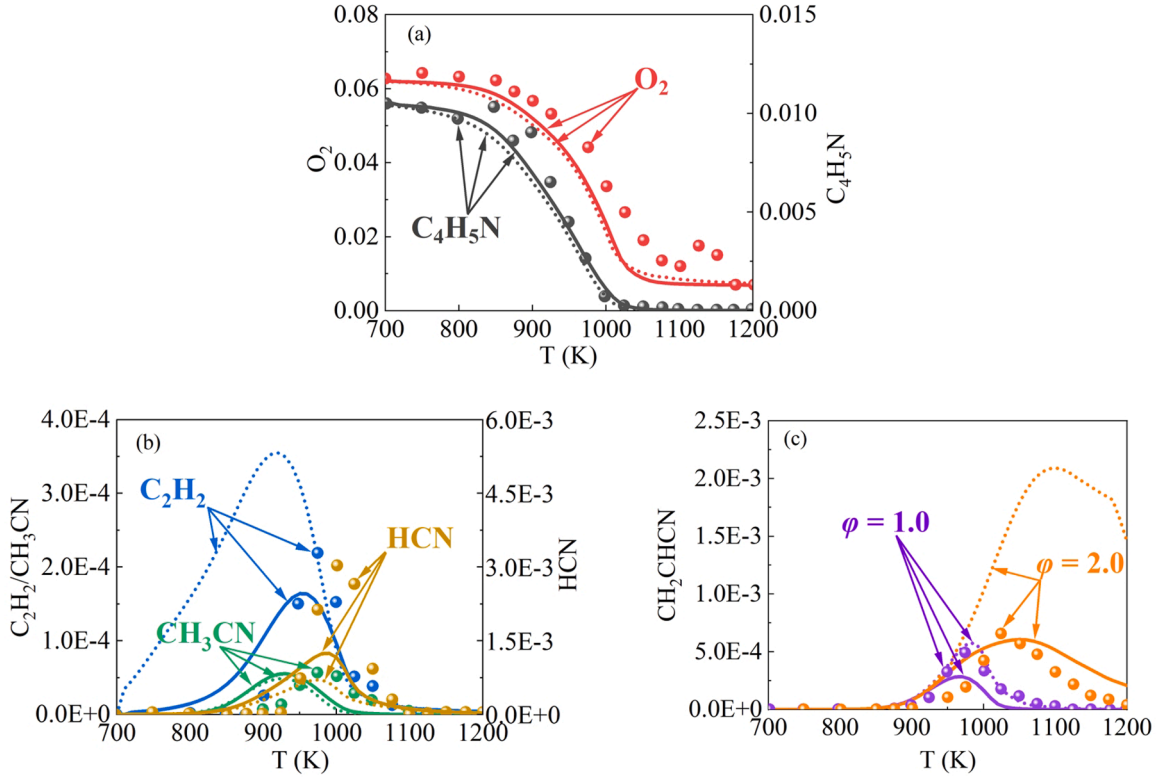

Fig. 2. The mole fractions of C_4H_5N, O_2, C_2H_2, HCN, CH_3CN in C_4H_5N oxidation at φ=1.0, and CH_2CHCN in C_4H_5N oxidation at φ=1.0 and 2.0. The values were calculated with base (dash line) and updated mechanism (solid line), along with the experimental results (scatter) in [23].

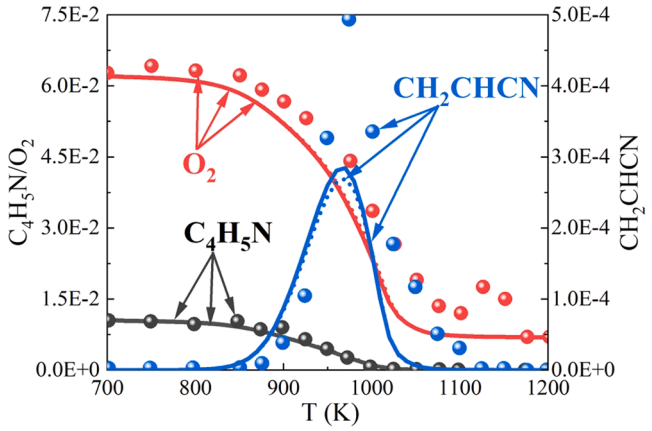

Fig. 3. The mole fractions of C_4H_5N, O_2 and CH_2CHCN calculated using the rate constants of four barrierless reactions obtained in this study and those in [23] at φ=1.0.

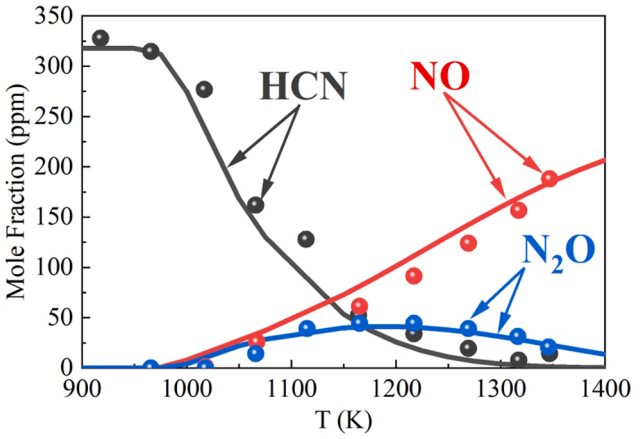

Fig. 4. Comparison of experimental results [26] and modeling predictions for HCN oxidation in a plug flow reactor.

comparison in the oxidation of HCN calculated with base and updated mechanisms was not carried out in this study. The exited mole fractions of HCN, predicted by the updated mechanism, within the temperature range of 900~1400 K, aligned well with the experimental results. At 1350 K, the modeled mole fraction of NO was 185.7 ppm, which was only 1.5 % smaller than the experimental result. Furthermore, the updated mechanism demonstrated good performance in predicting the yields of N_2O. The modeled peak mole fraction of N_2O was 41.2 ppm, which closely matched the experimental value of 44.4 ppm. Additionally, both the modeled and experimental peaks for the mole fraction of N_2O were observed around 1200 K.

The performance of the updated mechanism in predicting the formation of A1, one of the most significant precursors for soot formation, was illustrated in Fig. 5. The effect of C2-CN sub-mechanism on C_2H_2 oxidation can be ignored since there were no N-containing species generated in C_2H_2 oxidation process, thus only updated mechanism was adopted to simulate C_2H_2 oxidation. It was evident from Fig. 5 that the modeled results successfully captured the exit mole fractions of A1 at φ=2.0 and 3.0 over the temperature range of 600~1050 K. At 1050 K, the modeled mole fractions of A1 at φ=2.0 and 3.0 were 5.24×10^{-6} and 1.14×10^{-5}, respectively, which agreed well with the experimental results (5.61×10^{-6} at φ=2.0 and 1.48×10^{-5} at φ=3.0). Additionally, the experimental peak mole fractions of A1 at φ=0.5 and 1.0 were only around 1 ppm, significantly lower than those at φ=2.0 and 3.0. Therefore, the subsequent investigation focused only on the oxidation of

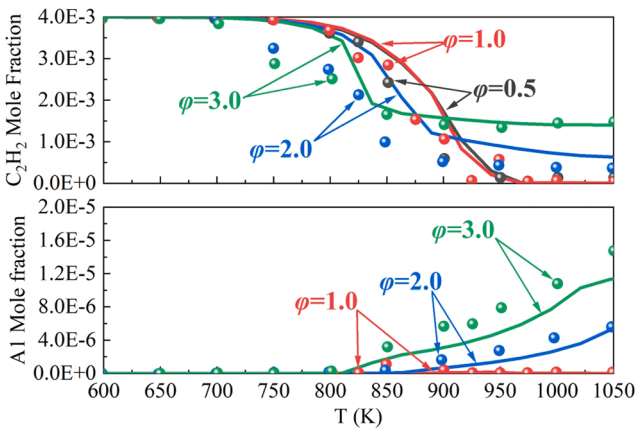

Fig. 5. Comparison of experimental results [43] and modeling predictions for C_2H_2 oxidation in a plug flow reactor at φ=0.5, 1.0, 2.0, and 3.0.

C_2H_2/HCN at φ=2.0 and 3.0.

3.2. Oxidation of C_2H_2/HCN in a PSR

Fig. 6 illustrated the mole fraction profiles of reactants and major products in the oxidation of C_2H_2/HCN with an equivalence ratio of 2.0, as predicted by the base and updated mechanisms. In Fig. 6(a), the oxidation of C_2H_2 initiated at 700 K and was nearly consumed at 1000 K. In Fig. 6(b), HCN began to react at 900 K, with only approximately half of the HCN consumed at 1500 K. The mole fraction of A1, as shown in Fig. 6(c), started to increase from 890 K and reached a peak value at 1100 K. The updated mechanism predicted a 9.1 % lower peak mole fraction of A1 compared to the base mechanism. In Fig. 6(d), the mole fraction of BGHIF, predicted by the base mechanism, peaked at 1.07×10^{-7} at 1150 K, which was 18.4 % higher than the value predicted by the updated mechanism. The mole fraction profiles of NO and N_2O were depicted in Fig. 6(e) and (f), respectively. Both NO and N_2O production commenced at 850 K, although the production rate of N_2O was lower than that of NO. The mole fraction of N_2O reached its peak value at 1020 K, while NO peaked at 900 K. The base and updated mechanisms provided similar predictions for NO production. Whereas, compared to the base mechanism, the updated mechanism yielded a relatively lower prediction for N_2O production. The peak mole fraction of N_2O predicted by the base mechanism was 2.69×10^{-5}, approximately 5.9 % higher than the value predicted by the updated mechanism.

The mole fraction profiles of C_2H_2, HCN, A1, BGHIF, NO, N_2O, H, OH, and O in the oxidation of C_2H_2/HCN with an equivalence ratio of 3.0, as predicted by the base and updated mechanisms, were compared in Fig. 7. The oxidation of C_2H_2 (Fig. 7(a)) initiated at 700 K, and at the temperature above 1100 K, approximately 17 % of C_2H_2 remained unoxidized due to the near depletion of O_2. HCN (Fig. 7(b)) started to oxidize at 860 K with an equivalence ratio of 3.0. The updated mechanism predicted a higher consumption rate of HCN than the base mechanism, especially at the temperature above 1100 K. Both the yields of A1 and BGHIF were underestimated by the updated mechanism than the base mechanism. The peak mole fractions of A1 and BGHIF predicted by the updated mechanism were 8.4 % and 13.6 % lower than those predicted by the base mechanism. Comparing Fig. 6(e) and 7(e) revealed that an increase in the equivalence ratio led to a larger difference in the peak mole fraction of NO predicted by the base and updated mechanisms. In Fig. 7(f), it was evident that the updated mechanism gave a lower prediction for the mole fraction of N_2O compared to the base mechanism in the temperature range from 880 K to 1310 K. The peak mole fraction of N_2O predicted by the updated mechanism was approximately 11.4 % lower than that predicted by the base mechanism. Fig. 7(g), (h), and (i) showed that there was little difference between the

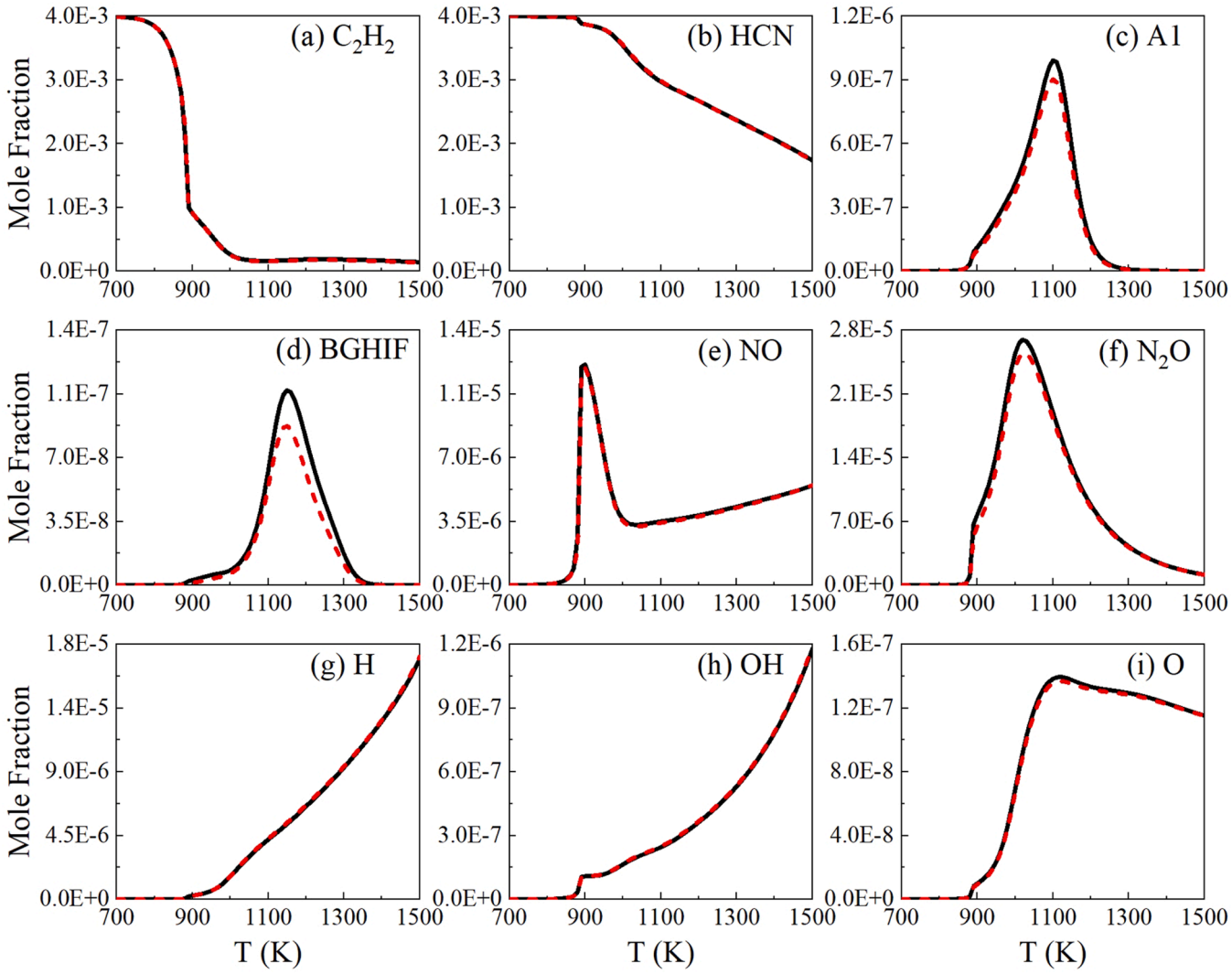

Fig. 6. The mole fraction profiles of (a) C_2H_2, (b) HCN, (c) A1, (d) BGHIF, (e) NO, (f) N_2O, (g) H, (h) OH and (i) O at φ=2.0, black solid line represents the base mechanism and red dash line represents the updated mechanism.

results obtained by the base and updated mechanisms when the temperature was below 1300 K. Nevertheless, above 1300 K, the production rates of H, OH, and O radicals predicted by the updated mechanism were improved, which contrasted with the trends observed for NO, N_2O, and PAHs.

3.2.1. *ROP and sensitivity analyses of BGHIF*

ROP and sensitivity analyses were conducted to elucidate the detailed formation pathways of BGHIF and NO/N_2O using the base and updated mechanisms. The temperatures chosen for the analyses were 1150 K (φ=2.0) and 1330 K (φ=3.0) for BGHIF, and 1020 K (φ=2.0) and 980 K (φ=3.0) for N_2O, corresponding to the temperatures at their peak mole fractions.

Based on the ROP results, the formation pathways of BGHIF calculated by the base and updated models were depicted in Fig. 8(a) and (b). In the base mechanism, the consumption of C_2H_2 at φ=2.0 and 3.0 was initiated through three different channels. The primary channel involved the oxidation of C_2H_2 by O radicals, forming HCCO (C_2H_2+O=HCCO+H), with integrated ROP values of 1.13×10^{-5} and 8.42×10^{-6} mol/cm^3 at φ=2.0 and 3.0, respectively. Two other major consumption channels of C_2H_2 were the combination reactions with CH_2 (C_2H_2+CH_2=C_3H_3+H) and CH_2 (S) (C_2H_2+CH_2(S)=C_3H_3+H) radicals, leading to the formation of C_3H_3. HCCO was converted to C_3H_3 through the reaction HCCO+C_2H_2=C_3H_3+CO. C_6H_6 was predominantly produced by the direct self-combination reaction of C_3H_3 at φ=3.0. However, at φ=2.0, the isomerization of fulvene following the self-combination reaction of C_3H_3 was another significant pathway for C_6H_6 formation. C_6H_6 underwent H-abstraction reactions, producing C_6H_5 radicals, or was directly converted to BGHIF via C_6H_6+A2R5-=BGHIF+H+H_2 at both φ=2.0 and 3.0. C_6H_5 was primarily converted to A1C2H via the reaction C_6H_5+C_2H_2=A1C2H+H, as well as through the pathway C_6H_5→C_7H_8→C_7H_7→A1C2H3→n-C_7H_8→A1C2H at φ=2.0. However, at φ=3.0, only the former pathway made a significant contribution to the formation of A1C2H. A1C2H was primarily converted to A3-through two channels at φ=2.0 and 3.0: one involved A1C2H→A2R5→A2R5-→A3-, and the other involved A1C2H→A2R5→A3→A3-. The formation of BGHIF at φ=2.0 and 3.0 mainly occurred through H-abstraction and C_2H_2-addition reactions from A3-.

Compared with the base mechanism, the updated mechanism included an additional reaction pathway in the consumption of C_2H_2 at φ=2.0 and 3.0. The pathway involved the formation of HC_3N through the combination of C_2H_2 and CN. The new pathway directly competed with the other three C_2H_2 consumption channels, leading to a decrease in their reaction rates. Consequently, the subsequent formation rates of C_6H_6 and A3- were limited, resulting in a decrease in the mole fraction of BGHIF. Approximately 77.2 % and 72.7 % of HC_3N were converted to HCCO at φ=2.0 and 3.0, respectively, which contributed to the

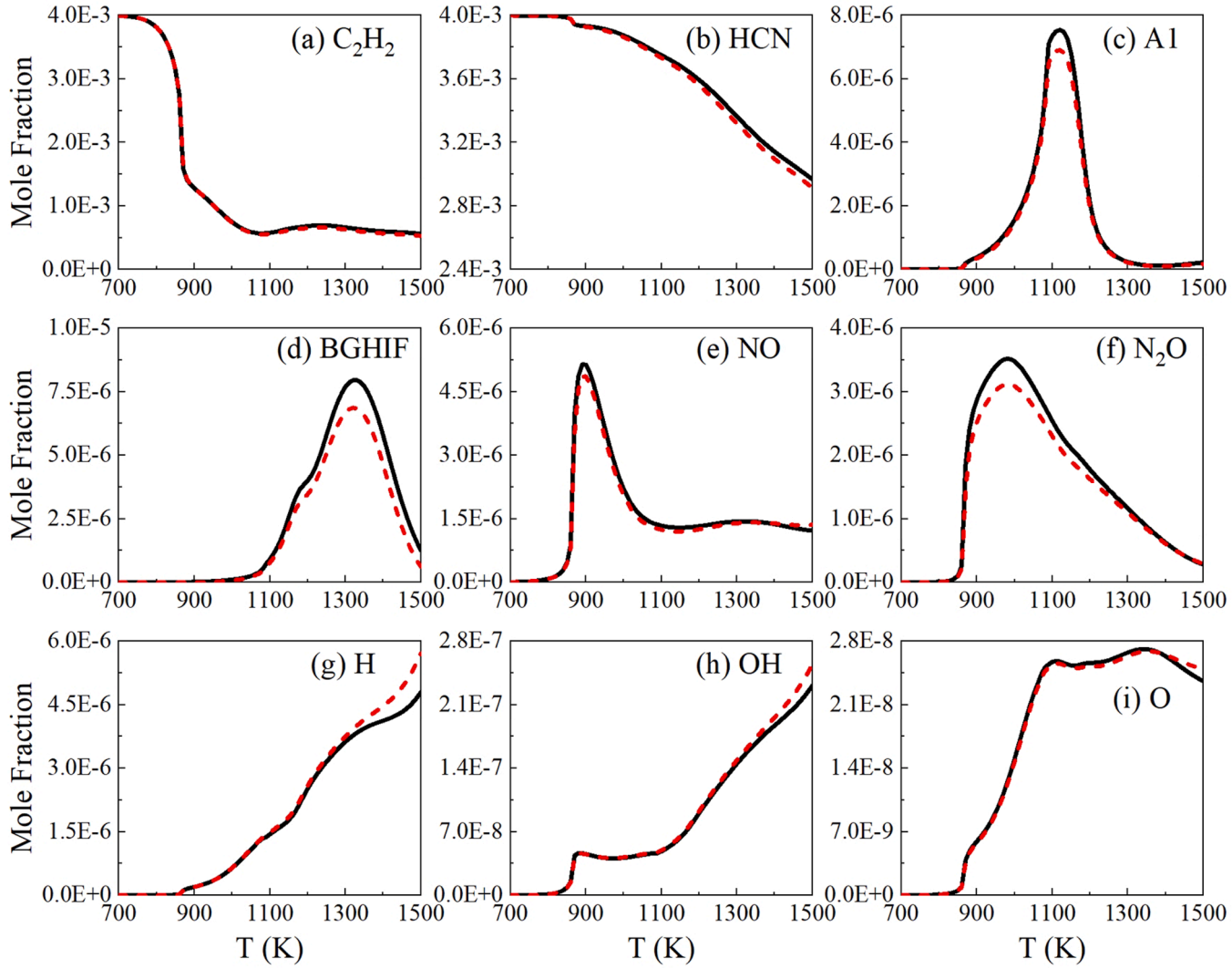

Fig. 7. The mole fraction profiles of (a) C_2H_2, (b) HCN, (c) A1, (d) BGHIF, (e) NO, (f) N_2O, (g) H, (h) OH and (i) O at φ=3.0, black solid line represents the base mechanism and red dash line represents the updated mechanism.

formation of BGHIF. Alongside HCCO, 19.3 % and 18.2 % of HC_3N were converted to HCCN at φ=2.0 and 3.0. Finally, the HCCN underwent oxidation to produce CO_2 through the reaction HCCN+O_2=CO_2+HCN.

The normalized sensitivity analyses of BGHIF, predicted by base and updated mechanisms at φ=2.0 and φ=3.0, were depicted in Fig. 9. From Fig. 9(a), it was evident that both the base and updated mechanisms yielded similar sensitivity analysis results for BGHIF. The reactions O+HCN=H+HNO and OH+CO=H+CO_2 were found to be the most sensitive reactions for BGHIF formation, as they produced highly reactive H radicals that promoted H-abstraction and C_2H_2-addition processes. However, compared to the base mechanism, the updated mechanism predicted higher values for the normalized sensitivity coefficients of O+HCN=H+HNO and OH+CO=H+CO_2. The reaction O+C_2H_2=H+HCCO was identified as the most sensitive reaction inhibiting the formation of BGHIF. This was because most of the HCCO produced in this reaction was converted to CO_2 via O_2+HCCO=H+CO+CO_2, thereby hindering the conversion of HCCO to C_3H_3. The sensitivity coefficient of O+C_2H_2=H+HCCO, as predicted by the updated mechanism, was 10 % smaller than that predicted by the base mechanism.

Fig. 9(b) showed that as the equivalence ratio increased from 2.0 to 3.0, the sensitivity coefficients for the five most important reactions decreased noticeably. The reaction CH_2+C_2H_2=H+C_3H_3 was identified as the most sensitive reaction for BGHIF formation, as it was a key reaction that consumed C_2H_2 and produced C_3H_3, a significant precursor for C_6H_6 and BGHIF formation. The reactions H+C_7H_7=C_7H_8 and H+C_3H_4-P=H_2+C_3H_3 were also identified as major promoting reactions for BGHIF formation at φ=3.0. Compared to the base mechanism, the updated mechanism predicted higher sensitivity coefficients for these three most important reactions in promoting BGHIF formation, similar to the case at φ=2.0. The reaction H+C_3H_3=C_3H_4-P exhibited the most inhibiting effect on BGHIF formation at φ=3.0, as it competed with C_6H_6 for the C_3H_3 radical. The updated mechanism provided a significantly higher prediction of the sensitivity coefficient for H+C_3H_3=C_3H_4-P than the base mechanism.

3.3. ROP and sensitivity analyses of NO/N_2O

Figs. 10(a) and (b) depicted the formation pathways of NO and N_2O predicted by the base and updated mechanisms at φ=2.0 and 3.0. In the base mechanism, the main consumption channel of HCN was its oxidation of O radical producing NCO. At φ=2.0 and 3.0, 48.9 % and 39.2 % of HCN were converted to NCO. CN was also an important product of HCN, which was generated via HCN+NCO=CN+HNCO and HCN+OH=H_2O+CN. CN was then mainly converted to NCO, and approximately 16 % and 21 % of CN were converted to NO at φ=2.0 and

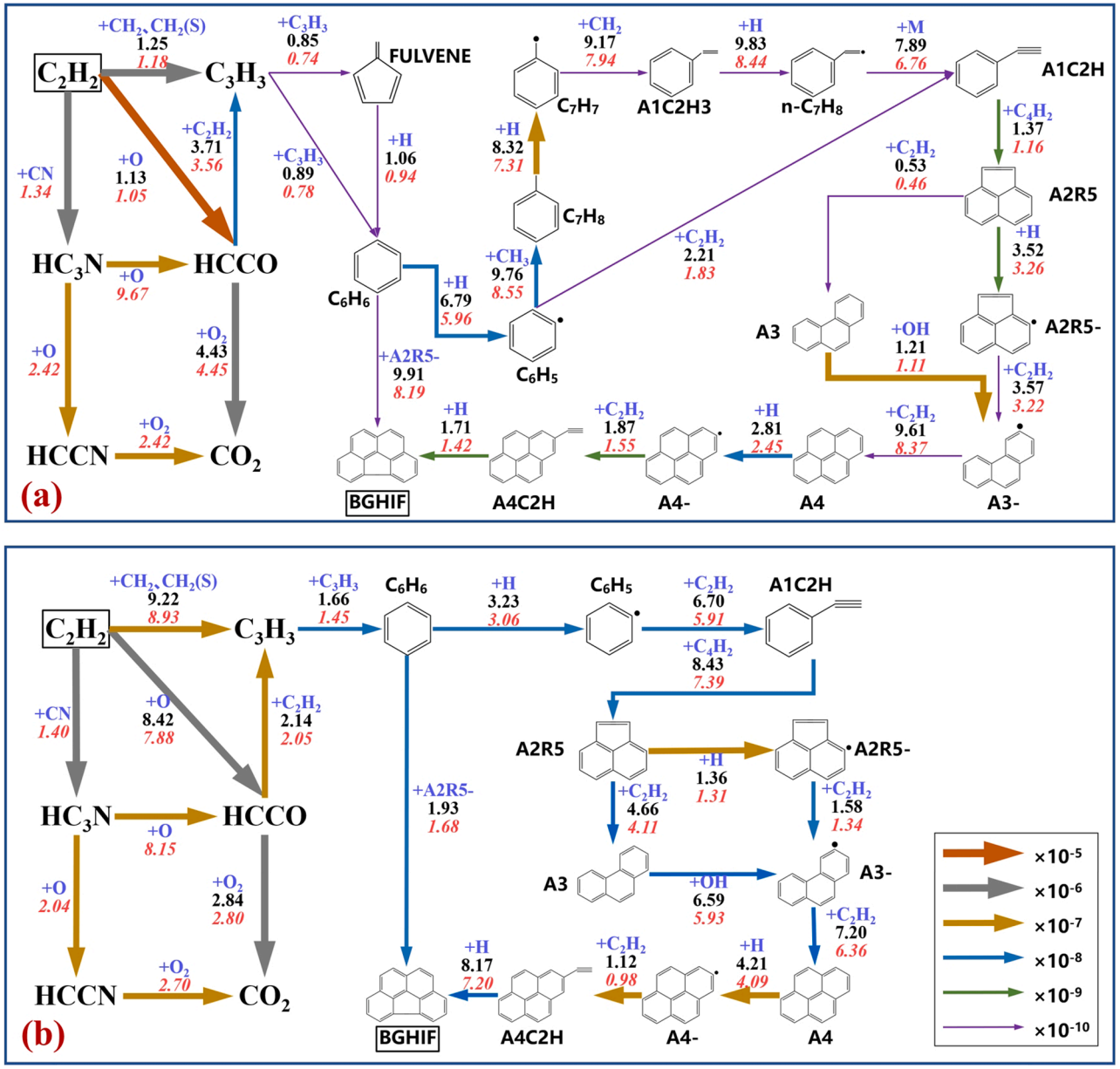

Fig. 8. Formation pathways of BGHIF formation at (a) φ=2.0 and (b) φ=3.0, the black and red numbers were the ROPs calculated by the base and updated mechanisms.

3.0, respectively. In Fig. 10(a), NCO was converted to HNCO via NCO+H_2 =H+HNCO at φ=2.0, which was subsequently converted to NO through the pathway of HNCO→NH_2→HNO→NO. At the equivalence ratio of 3.0, the reactions CH_2O+NCO=HCO+HNCO and C_2H_6+NCO=C_2H_5+HNCO played a dominant role in the formation of HNCO from NCO. Moreover, H_2NO was also a key intermediate in the formation of NO from NCO, which was mainly produced by NH_2 and converted to HNO. N_2O was mainly produced via NO+NH=N_2O+H at φ=2.0 and 3.0.

When considering the updated mechanism, an additional consumption channel of HCN was observed in Fig. 10(a) and (b), i.e., the combination reaction between HCN and C_2H_3 radical, yielding CH_2CHCN. As a result, the ROPs of HCN+NCO=CN+HNCO at φ=2.0 and 3.0 decreased by 4.1 % and 14.6 %, respectively. Interestingly, the ROPs of HCN+OH=H_2O+CN exhibited an inverse variation trend compared to HCN+NCO=CN+HNCO, which was due to the increase in mole fraction of OH radical shown in Fig. 6(h) and 7(h). From Fig. 10(a) and (b), the combination between CN and C_2H_2 became the most important consumption channel for CN, resulting in a decrease of 18.5 % (at φ=2.0) and 59.8 % (at φ=3.0) in the rate of CN+O_2=NO+CO. Around 69.3 % of HC_3N went back to CN via HC_3N+O=CN+HCCO at φ=2.0, which was higher than that at φ=3.0 (39.7 %). This illustrated the larger deviation between the mole fraction of NO predicted by the base and updated mechanisms at φ=3.0 (see Fig. 7(e)) than that at φ=2.0 (see Fig. 6(e)). At an equivalence ratio of 3.0, the rate of NO formation through the pathway of HNCO→NH_2→H_2NO→HNO→NO was also limited by CN+C_2H_2=HC_3N, leading to the ROP of HNO+CH_3=NO+CH_4 decreasing by 10.0 %.

As shown in Fig. 10(a) and (b), N_2O was mainly generated via NO+NH=N_2O+H at φ=2.0 and 3.0. At φ=2.0, the ROP of NO+NH=N_2O+H predicted by the updated mechanism was 5.4 % lower than that predicted by the base mechanism, and this difference increased to 11.4 % at φ=3.0. This explained why the difference between the peak mole fraction of N_2O modeled by the base and updated mechanism at φ=3.0 was larger than that at φ=2.0.

Fig. 11 compared the normalized sensitivity analyses of N_2O

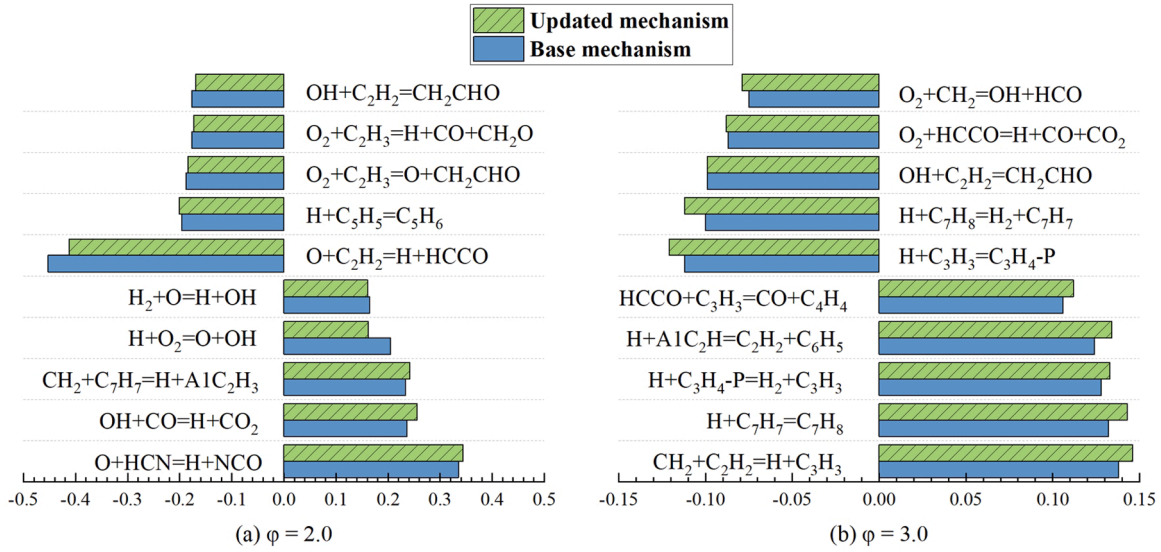

Fig. 9. Normalized sensitivity analyses of BGHIF at (a) φ=2.0 and (b) φ=3.0.

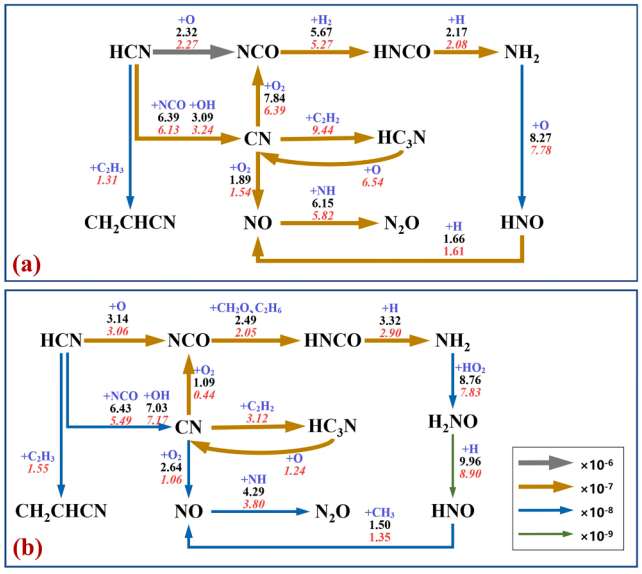

Fig. 10. Pathways of NO/N_2O formation at (a) φ=2.0 and (b) φ=3.0, the black and red numbers were the ROPs calculated by the base and updated mechanisms.

calculated using the base and updated mechanisms. As shown in Fig. 11 (a), $H+O_2=O+OH$ was the most sensitive reaction for promoting N_2O formation. This reaction produced reactive O and OH radicals, which increased the conversion ratio from HCN to NCO, NH_2 to HNO, and HC_3N to CN. Another significant sensitive reaction for N_2O formation was $NO+NH=H+N_2O$. The reaction $H+N_2O=N_2+OH$ exhibited the most significant inhibiting effect on N_2O formation. When the equivalence ratio increased from 2.0 to 3.0, the reaction $NO+NH=H+N_2O$ became the most sensitive reaction for N_2O formation. Reactions $O+HCN=CO+NH$ and $O_2+H_2CN=CH_2O+NO$ were also two major promoting reactions for N_2O formation, as they produced NH and NO, which were reactants in the reaction $NO+NH=H+N_2O$. The sensitivity coefficients of $O+HCN=CO+NH$ and $O_2+H_2CN=CH_2O+NO$ predicted by the updated mechanism were larger than those predicted by the base mechanism. The reaction $O+C_2H_2=H+HCCO$ was the most sensitive reaction for inhibiting N_2O formation, as it competed with the O radical in the reaction $HCN+O=NCO+H$, which was the most significant initial reaction for N_2O formation.

4. Conclusions

To better understand the pathways that impact the formation of NO/N_2O and PAHs in the combustion of hydrocarbon/NH_3 fuels, a detailed C2-CN sub-mechanism was developed and incorporated into the NOx/PAHs kinetic model. The rate constants for C_2H+CN, C_2H_3+CN, C_2H_5+CN, and CH_3+CH_2CN associations were updated by adopting the VRC-TST with M06–2X/def2-TZVP. The oxidation of C_2H_2/HCN in a PSR with φ=2.0 and 3.0 at the temperature range of 700~1500 K was simulated using base and updated mechanisms. Based on the ROPs calculated by base and updated mechanisms, the reaction pathways of NO/N_2O and BGHIF were established and the effect of C2-CN sub-mechanism on the formations of NO/N_2O and BGHIF was analyzed. The main conclusions of this study are as follows.

The calculated rate constants of C_2H_5+CN and CH_3+CH_2CN associations exhibited a positive dependence on temperature, while those of C_2H+CN and C_2H_3+CN showed a negative correlation with temperature.

The peak mole fractions of BGHIF at φ=2.0 and 3.0 predicted by the updated mechanism were 18.4 % and 13.6 % lower than those predicted by the base mechanism, indicating the suppressive effect of the C2-CN sub-mechanism on the PAHs formation. The inclusion of an additional consumption channel of C_2H_2 ($C_2H_2+CN=HC_3N+H$) was predicted by the C2-CN sub-mechanism limited the forward reaction rates of $C_2H_2+CH_2(S)=C_3H_3+H$ and $C_2H_2+CH_2=C_3H_3+H$ at φ=2.0 and 3.0, resulting in a decrease in the mole fraction of BGHIF.

At φ=2.0 and 3.0, the C2-CN sub-mechanism demonstrated a stronger suppressive effect on the formation of N_2O than NO. The limitation of C2-CN sub-mechanism on the NO/N_2O formation could be explained by an additional consumption channel of CN through $CN+C_2H_2=HC_3N+H$, consequently leading to a decrease in NO/N_2O via the reaction sequence $CN\rightarrow NO\rightarrow N_2O$ and $CN\rightarrow NCO\rightarrow HNCO\rightarrow NH_2\rightarrow HNO\rightarrow NO\rightarrow N_2O$. Additionally, the combination reaction between HCN and C_2H_3 radical, yielding CH_2CHCN, played a key role in reducing the mole fractions of NO and N_2O.

CRediT authorship contribution statement

Yu Yang: Writing – original draft. **Shu Zheng:** Conceptualization. **Huanhuan Wang:** Writing – review & editing. **Bin Hu:** Validation. **Hao Liu:** Methodology. **Ran Sui:** Formal analysis. **Qiang Lu:** Project

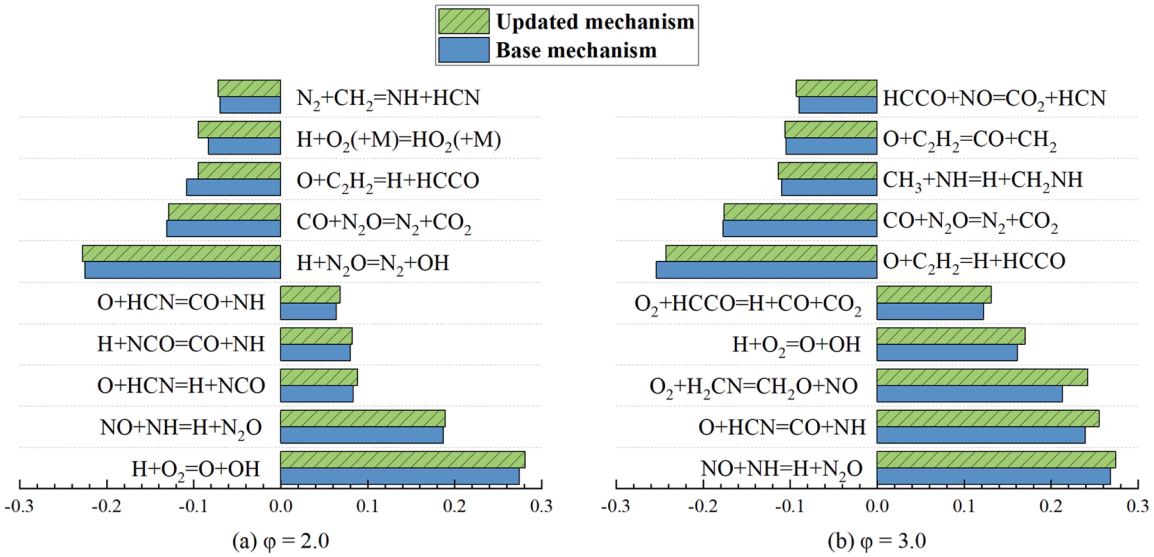

Fig. 11. Normalized sensitivity analyses of N_2O at (a) φ=2.0 and (b) φ=3.0.

administration.

Declaration of Competing Interests

The authors declare that they have no known competing financial interests or personal relationships that could have appeared to influence the work reported in this paper.

Acknowledgments

This work was supported by the National Key Research Development Program of China (No. 2022YFB4003901), the National Natural Science Foundation of China (Nos. 52276185, 52276189 and 52206157), the Natural Science Foundation of Jiangsu Province (No. BK20231209), and the Fundamental Research Funds for the Central Universities (No. 2023JC009).

Supplementary materials

Supplementary material associated with this article can be found, in the online version, at doi:10.1016/j.combustflame.2023.113267.

References

[1] A. Valera-Medina, F. Amer-Hatem, A. Azad, et al., Review on ammonia as a potential fuel: from synthesis to economics, Energy Fuel 35 (2021) 6964–7029.
[2] Y. Liu, X. Cheng, Y. Li, et al., Effects of ammonia addition on soot formation in ethylene laminar diffusion flames, Fuel 292 (2021), 120416.
[3] Y. Yang, S. Zheng, R. Sui, et al., Impact of ammonia addition on soot and NO/N_2O formation in methane/air co-flow diffusion flames, Combust. Flame 247 (2023) 112483.
[4] M. Frenklach, D.W. Clary, W.C. Gardiner Jr, et al., Detailed kinetic modeling of soot formation in shock-tube pyrolysis of acetylene, Symp. (Int.) Combust. 20 (1985) 887–901.
[5] H. Richter, J.B. Howard, Formation and consumption of single-ring aromatic hydrocarbons and their precursors in premixed acetylene, ethylene and benzene flames, Phys. Chem. Chem. Phys. 4 (2002) 2038–2055.
[6] A. Jerez, J.-L. Consalvi, A. Fuentes, et al., Soot production modeling in a laminar coflow ethylene diffusion flame at different Oxygen Indices using a PAH-based sectional model, Fuel 231 (2018) 404–416.
[7] Y. Yang, S. Zheng, Y. He, et al., Effects of simultaneous CO2 addition to the fuel and oxidizer streams on soot formation in co-flow diffusion ethylene flame, Fuel 353 (2023) 129181.
[8] S. Qi, Z. Sun, Z. Wang, et al., Effects of gas preheat temperature on soot formation in co-flow methane and ethylene diffusion flames, Proc. Combust. Inst. 38 (2021) 1225–1232.
[9] A. Nobili, A. Cuoci, W. Pejpichestakul, et al., Modeling soot particles as stable radicals: a chemical kinetic study on formation and oxidation. Part I. Soot formation in ethylene laminar premixed and counterflow diffusion flames, Combust. Flame 243 (2022), 112073.
[10] J. Appel, H. Bockhorn, M. Frenklach, Kinetic modeling of soot formation with detailed chemistry and physics: laminar premixed flames of C2 hydrocarbons, Combust. Flame 121 (2000) 122–136.
[11] A.M. Bennett, P. Liu, Z. Li, et al., Soot formation in laminar flames of ethylene/ammonia, Combust. Flame 220 (2020) 210–218.
[12] C. Zhang, L. Chen, S. Ding, et al., Effects of soot inception and condensation PAH species and fuel preheating on soot formation modeling in laminar coflow CH_4/air diffusion flames doped with n-heptane/toluene mixtures, Fuel 253 (2019) 1371–1377.
[13] J.A. Miller, C.T. Bowman, Mechanism and modeling of nitrogen chemistry in combustion, Prog. Energy Combust. 15 (1989) 287–338.
[14] S.J. Klippenstein, L.B. Harding, P. Glarborg, et al., The role of NNH in NO formation and control, Combust. Flame 158 (2011) 774–789.
[15] Y. Song, H. Hashemi, J.M. Christensen, et al., Ammonia oxidation at high pressure and intermediate temperatures, Fuel 181 (2016) 358–365.
[16] S. Arunthanayothin, A. Stagni, Y. Song, et al., Ammonia–methane interaction in jet-stirred and flow reactors: an experimental and kinetic modeling study, Proc. Combust. Inst. 38 (2021) 345–353.
[17] A. Konnov, I. Dyakov, J. De Ruyck, Probe sampling measurements of NO in CH_4+O_2+N_2 flames doped with NH_3, Combust. Sci. Technol. 178 (2006) 1143–1164.
[18] T. Mendiara, P. Glarborg, Ammonia chemistry in oxy-fuel combustion of methane, Combust. Flame 156 (2009) 1937–1949.
[19] P. Glarborg, J.A. Miller, B. Ruscic, et al., Modeling nitrogen chemistry in combustion, Prog. Energy Combust. 67 (2018) 31–68.
[20] M.J. Montgomery, H. Kwon, J.A. Dreyer, et al., Effect of ammonia addition on suppressing soot formation in methane co-flow diffusion flames, Proc. Combust. Inst. 38 (2021) 2497–2505.
[21] L. Herbert, I.W. Smith, R.D. Spencer-smith, Rate constants for the elementary reactions between CN radicals and CH_4, C_2H_6, C_2H_4, C_3H_6, and C_2H_2 in the range: 295⩽ T/K⩽ 700, Int. J. Chem. Kinet. 24 (1992) 791–802.
[22] A.F. Albernaz, W.B. da Silva, E. Correa, Isocyanoacetylene and cyanoacetylene formation study from C_2H_2+CN reaction, Int. J. Chem. Kinet. 54 (2022) 309–316.
[23] M. Pelucchi, S. Arunthanayothin, Y. Song, et al., Pyrolysis and combustion chemistry of pyrrole, a reference component for bio-oil surrogates: jet-stirred reactor experiments and kinetic modeling, Energy Fuel 35 (2021) 7265–7284.
[24] L.-N. Wu, Z.-Y. Tian, J.-J. Weng, et al., Experimental and kinetic study on the low-temperature oxidation of pyridine as a representative of fuel-N compounds, Combust. Flame 202 (2019) 394–404.
[25] J.C. Mackie, M.B. Colket, P.F. Nelson, Shock tube pyrolysis of pyridine, J. Phys. Chem. 94 (1990) 4099–4106.
[26] P. Glarborg, J.A. Miller, Mechanism and modeling of hydrogen cyanide oxidation in a flow reactor, Combust. Flame 99 (1994) 475–483.
[27] B. Long, Y. Wang, Y. Xia, et al., Atmospheric kinetics: bimolecular reactions of carbonyl oxide by a triple-level strategy, J. Am. Chem. Soc. 143 (2021) 8402–8413.
[28] J.L. Bao, X. Zhang, D.G. Truhlar, Barrierless association of CF_2 and dissociation of C_2F_4 by variational transition-state theory and system-specific quantum Rice–Ramsperger–Kassel theory, Proc. Natl. Acad. Sci. USA 113 (2016) 13606–13611.
[29] L. Zhang, D.G. Truhlar, S. Sun, Association of Cl with C_2H_2 by unified variable-reaction-coordinate and reaction-path variational transition-state theory, Proc. Natl. Acad. Sci. USA 117 (2020) 5610–5616.
[30] J. Giménez-López, A. Millera, R. Bilbao, et al., HCN oxidation in an O_2/CO_2 atmosphere: an experimental and kinetic modeling study, Combust. Flame 157 (2010) 267–276.

[31] P. Casavecchia, N. Balucani, L. Cartechini, et al., Crossed beam studies of elementary reactions of N and C atoms and CN radicals of importance in combustion, Faraday Discuss. 119 (2002) 27–49.
[32] K.K. Singh, P. Tandon, A. Misra, et al., Quantum chemical study on the formation of isopropyl cyanide and its linear isomer in the interstellar medium, Int. J. Astrobiol. 20 (2021) 62–72.
[33] N.A. Slavinskaya, U. Riedel, S.B. Dworkin, et al., Detailed numerical modeling of PAH formation and growth in non-premixed ethylene and ethane flames, Combust. Flame 159 (2012) 979–995.
[34] G. Capriolo, C. Brackmann, M.L. Lavadera, et al., An experimental and kinetic modeling study on nitric oxide formation in premixed C3 alcohols flames, Proc. Combust. Inst. 38 (2021) 805–812.
[35] A. Lifshitz, C. Tamburu, Thermal decomposition of acetonitrile. Kinetic modeling, Int. J. Chem. Kinet. 30 (1998) 341–347.
[36] J. Zheng, J.L. Bao, R. Meana-Pañeda, et al., Polyrate-version 2017-C, University of Minnesota, Minneapolis, 2017.
[37] M. Frisch, G. Trucks, H.B. Schlegel, et al., Gaussian 16, Gaussian, Inc, Wallingford, CT, 2016.
[38] Y. Zhao, D.G. Truhlar, The M06 suite of density functionals for main group thermochemistry, thermochemical kinetics, noncovalent interactions, excited states, and transition elements: two new functionals and systematic testing of four M06-class functionals and 12 other functionals, Theor. Chem. Acc. 120 (2008) 215–241.
[39] F. Weigend, R. Ahlrichs, Balanced basis sets of split valence, triple zeta valence and quadruple zeta valence quality for H to Rn: design and assessment of accuracy, Phys. Chem. Chem. Phys. 7 (2005) 3297–3305.
[40] J. Guo, S. Tang, N. Tan, Theoretical and kinetic study of the reaction of C_2H_3+HO_2 on the $C_2H_3O_2H$ potential energy surface, RSC Adv. 7 (2017) 44809–44819.
[41] A. Cuoci, A. Frassoldati, T. Faravelli, et al., OpenSMOKE++: an object-oriented framework for the numerical modeling of reactive systems with detailed kinetic mechanisms, Comput. Phys. Commun. 192 (2015) 237–264.
[42] P. Dagaut, P. Glarborg, M.U. Alzueta, The oxidation of hydrogen cyanide and related chemistry, Prog. Energy Combust. 34 (2008) 1–46.
[43] B.-Y. Wang, Y.-X. Liu, J.-J. Weng, et al., New insights in the low-temperature oxidation of acetylene, Proc. Combust. Inst. 36 (2017) 355–363.